Applied Radiation and Isotopes 197 (2023) 110828

Contents lists available at ScienceDirect

Applied Radiation and Isotopes

journal homepage: www.elsevier.com/locate/apradiso

Analysis of a neutron-induced conversion electron spectrum of gadolinium

S. Pommé [a,*], M.C. Veale [b], D.E. Pooley [c], F. Van Assche [d], F. Falksohn [e], S.M. Collins [e,f]

[a] European Commission, Joint Research Centre (JRC), Geel, Belgium
[b] Technology Department, Rutherford Appleton Laboratory (STFC), Oxfordshire, UK
[c] ISIS Neutron and Muon Source, Rutherford Appleton Laboratory (STFC), Oxfordshire, UK
[d] Ghent University (UGent), Gent, Belgium
[e] National Physical Laboratory (NPL), Teddington, UK
[f] School of Mathematics and Physics, University of Surrey, Guilford, UK

ARTICLE INFO

Keywords:
Internal conversion
Electron emission probability
Gadolinium
Neutron capture
Neutron imaging

ABSTRACT

A 100-nm-thick gadolinium layer deposited on a pixelated silicon sensor was activated in a neutron field to measure the internal conversion electron (ICE) spectrum generated by neutron capture products of ^{155}Gd and ^{157}Gd. The experiment was performed at the ISIS neutron and muon facility, using a bespoke version of the HEXITEC spectroscopic imaging camera. Signals originating from internal conversion electrons, Auger electrons, x rays and gamma rays up to 150 keV were identified. The ICE spectrum has an energy resolution of 1.8–1.9 keV at 72 keV and shows peaks from the K, L, M, N+ ICEs of the 79.51 keV and 88.967 keV 2^+-0^+ gamma transitions from the first excited states in ^{158}Gd and ^{156}Gd, respectively, as well as the K ICEs of the 4^+-2^+ transitions at 181.931 keV and 199.213 keV from the respective second excited states. Spectrum analysis was performed using a convolution of a Gaussian with exponential functions at the low and high energy side as the peak shaping function. Relative ICE intensities were derived from the fitted peak areas and compared with internal conversion coefficient (ICC) values calculated from the BrIcc database. Relative to the dominant L shell contribution, the K ICE intensity conforms to BrIcc and the M, N, O+ ICE intensities are somewhat higher than expected.

1. Introduction

Gadolinium (Gd) is a rare earth element with an exceptionally high interaction probability with neutrons at thermal energy, specifically due to two of its seven stable isotopes ^{157}Gd (15.65% abundance, 254000 b cross section) and ^{155}Gd (14.8%, 60900 b) (Dumazert et al., 2018). Weighted by isotopic abundance, a natural Gd mixture has a thermal neutron cross section of 48800 (150) b, to which ^{157}Gd contributes by 81.5% and ^{155}Gd by 18.5% and the other isotopes by a negligibly small fraction (0.010%). Owing to this physical property, Gd is extremely useful as a neutron poison in nuclear power reactors as well as a neutron converter in nuclear instrumentation for neutron detection (Kandlakunta et al., 2013; Kandlakunta and Cao, 2012; Pfeifer et al., 2017; Dumazert et al., 2018, 2020, 2022). Dumazert et al. (2018) presented an extensive overview of physicochemical properties of Gd and the radioactive cascade that follows Gd(n,γ) reactions, including emissions of Auger electrons, internal conversion electrons (ICEs), x rays and gamma rays. The electron emissions are of additional interest to gadolinium neutron capture therapy (NCT) of cancer (Sakurai and Kobayashi, 2002; Cerullo et al., 2009; Narmani et al., 2018). Its paramagnetic properties make gadolinium useful as a contrast medium for magnetic resonance imaging (MRI) and it can be incorporated in nanoparticles with other agents for multifunctional diagnosis and therapy (Tian et al., 2015; Narmani et al., 2018).

Helium-3 is the most commonly deployed converter in neutron counters, owing to its large thermal neutron capture cross section and insensitivity to gamma radiation. However, its cost has risen due to a worldwide shortage, which has triggered research on alternative detection techniques using gadolinium (Kandlakunta et al., 2013; Dumazert et al., 2018). Neutron detectors must be designed specifically to detect neutrons and not be triggered by competing gamma ray fields that may overwhelm the detector and obscure the neutron signal. A desired quality is that charged particles are being produced by the neutron capture which can generate a dense cloud of charge carriers in a detector medium, e.g. a gas or thin semiconductor, whereas gamma rays pass mostly undetected (Masaoka et al., 2003; Kandlakunta and Cao, 2012). While the deexcitation of ^{158}Gd and ^{156}Gd reaction products is dominated by abundant electromagnetic radiations following

* Corresponding author.
E-mail address: stefaan.pomme@ec.europa.eu (S. Pommé).

https://doi.org/10.1016/j.apradiso.2023.110828
Received 13 February 2023; Received in revised form 25 March 2023; Accepted 17 April 2023
Available online 20 April 2023

rearrangements at nuclear and atomic level, the emission of conversion electrons is of particular interest for interference-free neutron detection. Gamma transitions between the first excited states of ^{158}Gd – from 4+ to 2+ and from 2+ to 0+ ground state – are responsible for 96.7% of the energy carried by internal conversion electrons after the ^{157}Gd(n,γ) reaction (Kandlakunta, 2012) and the case of ^{156}Gd is similar.

The gamma transitions of primary interest for neutron detection are those of 79.51 keV (α_T = 5.93) and 181.931 keV (α_T = 0.305) from ^{158}Gd, as well as 88.967 keV (α_T = 3.88) and 199.213 keV (α_T = 0.225) from ^{156}Gd. The associated internal conversion electrons are ejected from their orbital position around the atom with an energy equal to the gamma transition energy minus the electron shell binding energy. Table 1 gives an overview of the ICE spectra for the 79.51 keV and 88.967 keV E2 transitions. The internal conversion coefficients (ICC) have been obtained from interpolations of tables of Band et al. (2002) through the computer code BrIcc (Kibédi et al., 2008), using the "frozen orbital" approximation. As a further step in the deexcitation process, also characteristic low-energy x rays and Auger electrons are emitted. The main low-energy electron emission spectrum is comprised in the 4–200 keV range. The major Auger electron peak can be expected at 34.9 keV, the transition energy between L and K shells minus the L binding energy.

In many cases, BrIcc provides good estimates of the relative and absolute ICE emission probabilities, as was recently demonstrated for the main gamma lines from ^{234,235,236}U produced by the alpha decay of ^{238,239,240}Pu (Pommé et al., 2018). A counterexample is the 59 keV transition following alpha decay of ^{241}Am, where a nuclear penetration effect leads to anomalous ICC values (Pommé et al., 2019). Few ICE energy spectra of irradiated Gd have been published in the literature (Masaoka et al., 2003; Kandlakunta et al., 2013) and their energy resolution is rather low. In this work, a thin gadolinium layer deposited on a pixelated, low-noise, high-resolution, broad energy range silicon sensor was activated in a neutron field to measure the ICE spectrum up to 150 keV. The ICE spectrum has an energy resolution of 1.8–1.9 keV FWHM at 72 keV and shows peaks from the K, L, M, N+ ICEs of the 79.51 keV and 88.967 keV 2^+-0^+ gamma transitions from the first excited states in ^{158}Gd and ^{156}Gd, respectively, as well as the K ICEs of the 4^+-2^+ transitions at 181.931 keV and 199.213 keV from the respective second excited states. Spectrum analysis was done to compare relative peak areas with ratios of ICC values derived from the BrIcc database (Table 1).

Table 1
Energy of ICEs associated with the 79.51 keV and 88.967 keV gamma transitions of ^{158}Gd and ^{156}Gd, respectively, the predicted Internal Conversion Coefficients (ICC) from the BrIcc database, and the corresponding relative intensities normalised to 100%.

Shell	^{158}Gd - 79.51 keV			^{156}Gd - 88.967 keV		
	Energy	ICC	**I/ΣI**	**Energy**	ICC	**I/ΣI**
	keV	(−)	%	keV	(−)	%
K	**29.27**	**2.02**	**34.04**	**38.73**	**1.559**	**40.20**
L/K		1.50			1.15	
L1	71.13	0.1776	2.99	80.59	0.1381	3.56
L2	71.58	1.362	22.95	81.04	0.803	20.70
L3	72.27	1.482	24.97	81.72	0.848	21.86
L	**71.89**	**3.02**	**50.89**	**81.33**	**1.79**	**46.15**
L1/L3		0.120			0.163	
L2/L3		0.919			0.947	
M1	77.63	0.0379	0.64	87.09	0.0292	0.75
M2	77.82	0.316	5.33	87.28	0.187	4.82
M3	77.97	0.354	5.97	87.42	0.203	5.23
M4	78.29	0.00331	0.06	87.75	0.00184	0.05
M5	78.32	0.00328	0.06	87.78	0.00180	0.05
M	**77.89**	**0.714**	**12.03**	**87.34**	**0.423**	**10.91**
M1-3	77.88	0.7079	11.93	87.33	0.4192	10.81
M4-5	78.30	0.0066	0.11	87.76	0.0036	0.09
L/M		4.23			4.23	
N1	79.13	0.00874	0.15	88.59	0.00672	0.17
N2	79.22	0.0704	1.19	88.68	0.0416	1.07
N3	79.24	0.0785	1.32	88.70	0.0451	1.16
N4	79.36	0.000731	0.012	88.82	0.000408	0.011
N5	79.38	0.000706	0.012	88.83	0.000388	0.010
N6	79.51	$1.50\ 10^{-6}$	0.00003	88.97	$7.47\ 10^{-7}$	0.00002
N7	79.51	$1.76\ 10^{-6}$	0.00003	88.97	$8.74\ 10^{-7}$	0.00002
N	**79.23**	**0.1592**	**2.68**	**88.68**	**0.0942**	**2.43**
L/N		19.0			19.0	
O1	79.43	0.001374	0.023	88.93	0.001057	0.027
O2	79.49	0.00942	0.16	88.94	0.00556	0.14
O3	79.49	0.00984	0.17	88.95	0.00565	0.15
O4	79.50	$3.86\ 10^{-5}$	0.001	88.96	$2.15\ 10^{-5}$	0.001
O	**79.49**	**0.0207**	**0.35**	**88.94**	**0.01229**	**0.32**
L/O		146			146	
P	**79.50**	**$9.93\ 10^{-5}$**	**0.0017**	**88.96**	**$7.64\ 10^{-5}$**	**0.0020**
L/O+		145			145	
Total		**5.93**			**3.88**	

2. Methodology

2.1. The ICE spectrum

The neutron imaging detector used here consists of a Si hybrid pixel detector on which a layer of gadolinium is deposited. Thermal neutrons captured by the gadolinium produce a mixture of photons (gamma rays, x rays) and electrons (Auger, ICE). The sensor thickness is chosen such that electrons are detected and absorbed in the active volume, whereas high-energy photons have a low attenuation in the Si crystal, thus a high probability of leaving it without creating a measurable signal. As a result, the majority of the signals created in the sensor is generated by internal conversion electrons, especially those with energies below 100 keV.

Use was made of a bespoke HEXITEC system (high-energy x-ray imaging technology) (Veale et al., 2018) containing a 500-μm-thick, 80 × 80 pixel Si sensor with a pixel pitch of 250 μm (Cline et al., 2022) operated at a high frame rate of 9 kHz using the SpeXIDAQ data acquisition framework (Van Assche et al., 2021). Each pixel has a charge sensitive amplifier, leakage compensation circuit, shaping amplifier, and peak-track-and-hold circuit. A 100 nm layer of natural gadolinium was sputtered on top of the sensor entrance window prior to assembly. The sensor was exposed to pulses of thermal neutrons with energies 0.5–100 meV from the LOQ facility (Heenan et al., 1997) at the ISIS neutron and muon source. An individual frame of data consists of the energy deposited in each pixel. The resulting photon and electron spectrum was compiled from over 3×10^8 frames of data (9 h). Full details of the development of the novel neutron detector and the experimental test will be described elsewhere (Veale et al., 2023).

Fig. 1 shows the energy spectrum of events that were fully registered in single pixels only. The electron energy resolution – about 1.8 keV FWHM at 72 keV – is sufficiently good to discern well-defined peaks from the K, L and M+ shells, as well as Auger electrons and x rays (the latter with 0.8 keV FWHM peak width). This spectrum is of significantly higher quality than other Gd ICE spectra published in the literature. However, the ionisation track of the electrons (or photons) may create a charge cloud of comparable dimensions as the pixel size (250 μm) of the detector (Veale et al., 2014). Consequently, there is a significant number of events that are partially registered in 2, 3, or 4 adjacent pixels and sometimes even more.

Fig. 2 shows the aligned energy spectra deduced from events captured in 1, 2, 3 and 4 pixels and their relative contribution to the sum spectrum. For low-energy particles, the charge is mostly collected on single pixels. The multiplicity of pixels involved grows at higher energies due to elongation of the ionisation tracks and broadening of the charge cloud resulting from considerable scatter of the electrons in the silicon. Even though the single-pixel spectrum in Fig. 1 has the best energy resolution, spectral analysis is preferably performed on the sum spectrum in Fig. 2 to avoid significant spectral distortion as a function of energy. This comes at the cost of some deterioration of the energy

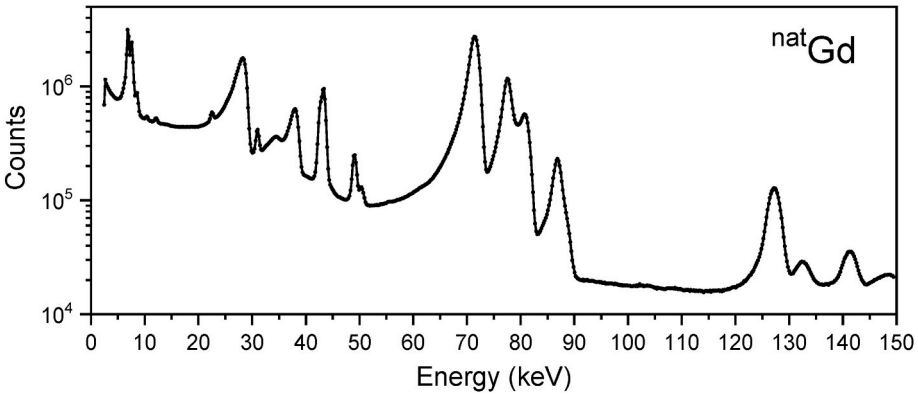

Fig. 1. The energy spectrum obtained from electrons and photons emitted in the deexcitation process of natural gadolinium after irradiation with thermal neutrons, exclusively registered as 'single-pixel events' in a pixelated silicon sensor.

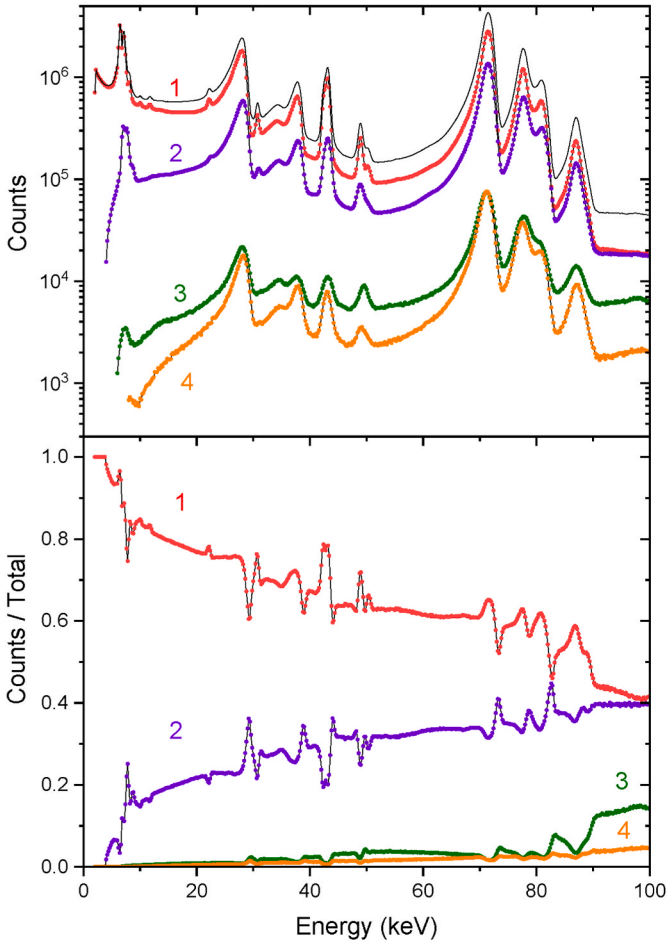

Fig. 2. Top: Energy spectra obtained from 'single-pixel' events (1) and from coincident events in 2, 3, or 4 adjacent pixels. The thin line on top represents the sum of these spectra. Bottom: Fractional contribution of each spectrum to the sum. Higher-order multiplicity events involving more than 4 pixels have an insignificantly low yield.

resolution– about 1.9 keV at 72 keV – and spectral misalignment above 100 keV.

2.2. Spectral analysis

The JRC has experience with ICE spectrometry using Peltier-cooled silicon drift detectors (Peräjärvi et al., 2014; Pommé et al., 2016; Pommé, 2022) and data analysis of Pu and Am ICE spectra (Pommé et al., 2018, 2019; Lützenkirchen et al., 2019). Spectrum fitting is done by means of the software utility 'BEST' (Pommé and Caro Marroyo, 2015), which was originally designed for alpha-particle spectrometry (see e.g. Marouli et al., 2017; García-Toraño et al., 2019). The peak shaping function is a convolution of a Gaussian with exponential tailing functions at the low and high energy side. Additionally, the software allows for photon peaks (x rays and gamma rays) to be fitted with Gaussian or pseudo-Voigt functions on an independent energy scale from the ICE peaks, since the electron peaks are generally shifted to lower energy values due to energy loss. Relative ICE intensities are derived from the peak areas and compared with ICC values from BrIcc (Table 1). The peak areas have not been corrected for a possible energy dependence of the counting efficiency.

2.3. Uncertainty estimation

Since there is a high level of spectral interference among the peak functions, uncertainty calculations on the peak intensities must take correlation effects into account (Pommé, 2015). Three major components are considered in this work:

$$u^2(I_k) = u^2_{\text{stat}} + u^2_{\text{intf}} + u^2_{\text{eff}} \tag{1}$$

in which u_{stat} refers to statistical uncertainties, u_{intf} to (anti-)correlated uncertainties due to peak and tailing interferences, and u_{eff} to uncertainties due to energy dependency in the detection efficiencies.

The u_{eff} value was roughly estimated by assuming a linear energy dependence of the detection efficiency by 0.1% per 1 keV distance from the peak of the L shell. This has an impact on the relative uncertainty of the L/K peak ratio by more than 4%. The relative uncertainty contribution is relatively small for the other shells (<0.8%) and negligible within the L subshell, considering the proximity of these peaks.

For the u_{stat} contribution, the statistical uncertainty for a peak area A_k was approximated through

$$u_{\text{stat}}(A_k) = \sqrt{A_k + 2\cdot\left(A^t_k + A^f_k\right)} \tag{2}$$

in which A^t_k is the (tailing) fraction of the interfering peaks underneath the central part of peak k, and A^f_k represents errors due to imperfections in the peak modelling, taken as the sum of the absolute values of the fit residuals within $\pm 2 \times$ FWHM of the peak top. The relative intensities I_k over all shells (or among the L subshells) are normalised to 100% and the propagation formula for independent uncertainties (Pommé, 2015) is applied for u_{stat}

$$u^2(I_k) = I_k^2(1-I_k)^2\left(\frac{u^2(A_k)}{A_k^2} + \frac{u^2\left(\sum_{i\neq k}A_i\right)}{\left(\sum_{i\neq k}A_i\right)^2}\right) \quad (3)$$

Eq. (3) sums the relative uncertainties of the area of peak k as well as the sum of the other peaks which make up 100%. The resulting statistical uncertainty is negligibly low (≪0.1%) owing to the extremely high counting precision in each bin of the ICE spectrum.

The most dominant uncertainty component is derived from interference among the ICE and photon peaks. The systematic uncertainty on the interference from peaks i underneath the peak k was estimated as 3% of their area in the region of ±2 × FWHM around the top of peak k. The most cautious propagation factor is used, assuming by default that all these interfering areas are in full anti-correlation (Pommé, 2015)

$$u^2(I_k) = \left(\frac{u^2_{intf}(A_k)}{\left(\sum_i A_i\right)^2}\right) \quad (4)$$

In the calculations of peak ratios (e.g. L/K, M/K, L1/L3), the relative uncertainties of both variables were simply summed, compatible with a worst-case scenario of full anti-correlation (as opposed to a quadratic sum of independent variables).

3. Results

3.1. L, M, N, O+ ICE intensities

The energy region between 60 keV and 90 keV is composed of a plethora of ICE peaks from the L-P shells of the 79.51 keV and 88.967 keV gamma transitions. Fig. 3 shows a first attempt to fit this part of the spectrum using fixed ratios in the subshells (i.e. L1/L3, L2/L3, M1/M3, etc.) as derived from the BrIcc data in Table 1. Since the transitions are not fully converted, Gaussian peaks representing the gamma rays were included in the fit. The resulting relative yields of the L, M, N and O+ ICE peaks are reported in Table 2 ("Fit 1").

No arbitrary 'background' function was used to fit the continuum underneath the peaks. The spectrum was fully composed of equally shaped Gaussian peaks convoluted with three left-handed exponential

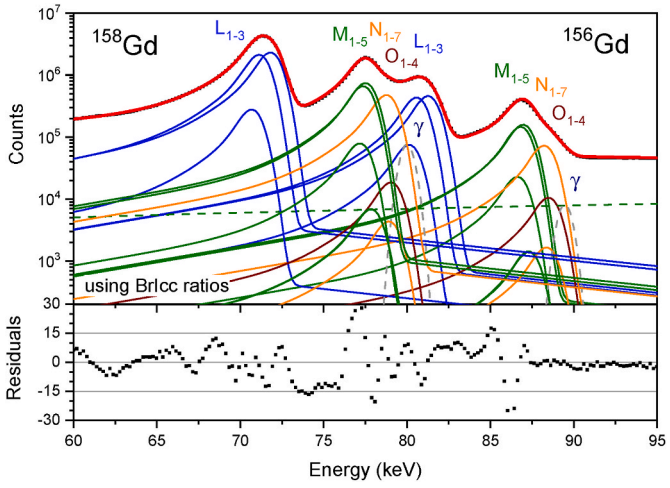

Fig. 3. Fit to the energy spectrum of L, M, N, O+ ICEs associated with the 79.51 keV and 88.967 keV transitions of ^{158}Gd and ^{156}Gd respectively, using fixed ICC subshell ratios as predicted from the BrIcc database. The dashed lines show contributions from the gamma rays and from interfering parts of the spectrum. The residuals of the fits are expressed in standard uncertainty of the number of counts in each bin.

Table 2
Fitted relative ICE peak areas from the 79.51 keV and 88.967 keV transitions of ^{158}Gd and ^{156}Gd, respectively, compared to expected ICC ratios from the BrIcc database. In "Fit 1", within each shell the relative peak contributions from subshells were set equal to the BrIcc ratios, whereas in "Fit 2" they were fitted without constraints. The digits of the standard uncertainties in parenthesis correspond with the last significant digits of the variable.

Ratio	^{158}Gd - 79.51 keV			^{156}Gd - 88.967 keV		
	BrIcc	Fit 1	Fit 2	BrIcc	Fit 1	Fit 2
L1/L3	0.120	0.120	0.10 (7)	0.163	0.163	0.01 (18)
L2/L3	0.919	0.919	0.86 (7)	0.947	0.947	0.92 (24)
L/K	1.50	1.53	1.55 (8)	1.15	1.17	1.14 (14)
L/M	4.23	3.16	3.08 (12)	4.23	2.94	2.85 (24)
L/N	19.0	9.8	13.1 (31)	19.0	13.0	13.8 (38)
L/O+	145	250	50 (50)	145	92	42 (40)

tailing functions and two right-handed tailing functions. The latter seemed a necessary feature, because the continuum parts of the spectrum show a negative slope at the high-energy side of the peaks. The fit in this 30-keV-wide energy region is complicated by the fact that the actual peak shapes vary smoothly with energy, due to differences in stopping power. Applying an identical peak shape over the whole energy spectrum leads to significant incompatibilities.

The quality of the fit in Fig. 3 is moderately good, but not satisfactory. This may suggest that the BrIcc ratios are not fully realistic, or that the measured spectrum is somewhat distorted. Prior experience with fits to ^{241}Am spectra has shown that consistent results could be obtained with energy resolutions of 0.65 keV, 0.8 keV and 1 keV FWHM, whereas spectra with 1.5 keV resolution could not warrant sufficient quality (Pommé et al., 2019). By examination of the width of fitted peaks, the electron energy resolution of the composite Gd spectrum could be estimated as 1.9 keV FWHM at 72 keV. Consequently, the ICCs derived from the fits in this work may be indicative of the real value but should carry a notable uncertainty.

In a second spectral analysis, the individual subshell peak areas were fitted freely, thus lifting the condition to conserve the BrIcc ratios. A linear energy calibration was maintained, even though some deviation from linearity may be anticipated in reality. The photon peaks were expanded with some symmetric tailing through an unnormalised pseudo-Voigt function

$$V_p(x,\sigma) = A\left[G(x,\sigma) + I \Big/ (1 + x/\gamma)^2\right] \quad (5)$$

in which $G(x,\sigma)$ is the Gaussian distribution as a function of distance from the centre and the standard deviation, the second term is a Cauchy distribution, and A, γ and I are height, width and relative weight parameters, respectively.

The residuals from the fit, shown in Fig. 4, are strongly reduced by the added freedom. The statistical accuracy in the bins is of the order of 0.05%, which explains why it is extremely difficult to achieve a perfect fit within 1–3 standard deviations with simple shape functions. In the graph, the contributions of subshells are summed to show the combinatory ICE energy peak from each shell. The relative peak areas and their standard uncertainty are listed in Table 2 ("Fit 2").

The relatively high fit results for the O+ ICE peak areas may be caused by the spectral broadening introduced by the multiple-pixel spectra which are not perfectly aligned with the single-pixel spectrum (Fig. 2). A fit to the single-pixel event spectrum has a slightly better energy resolution, which results in lower O+ contributions closer to the BrIcc values.

3.2. K ICE intensities

Due to energy straggling, the K ICE spectrum had to be analysed separately with different shaping parameters. Therefore the K peak areas could not be compared directly with the L shell peaks through the ratio

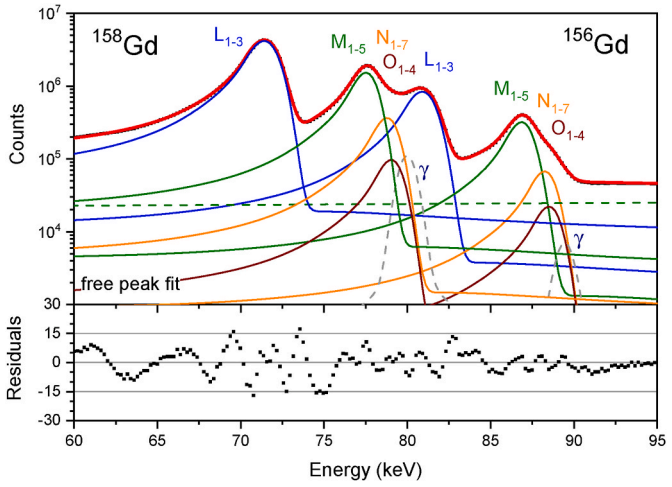

Fig. 4. Fit to the energy spectrum of L, M, N, O+ ICEs associated with the 79.51 keV and 88.967 keV transitions of ^{158}Gd and ^{156}Gd respectively. The subshells peaks were fitted independently and then summed into a combinatory peak. The dashed lines show contributions from the gamma rays and from interfering parts of the spectrum. The residuals of the fits are expressed in standard uncertainty of the number of counts in each bin.

of their amplitudes. The L/K ratio was determined by integrating the K and L peak areas over 2 × FWHM around their top. One of several possible peak fits is shown in Fig. 5. Interpretation of the fit results is complicated by a few obstacles. Despite their proximity, there may be a difference in width (about 2.5 keV) and tailing between the K ICE peaks

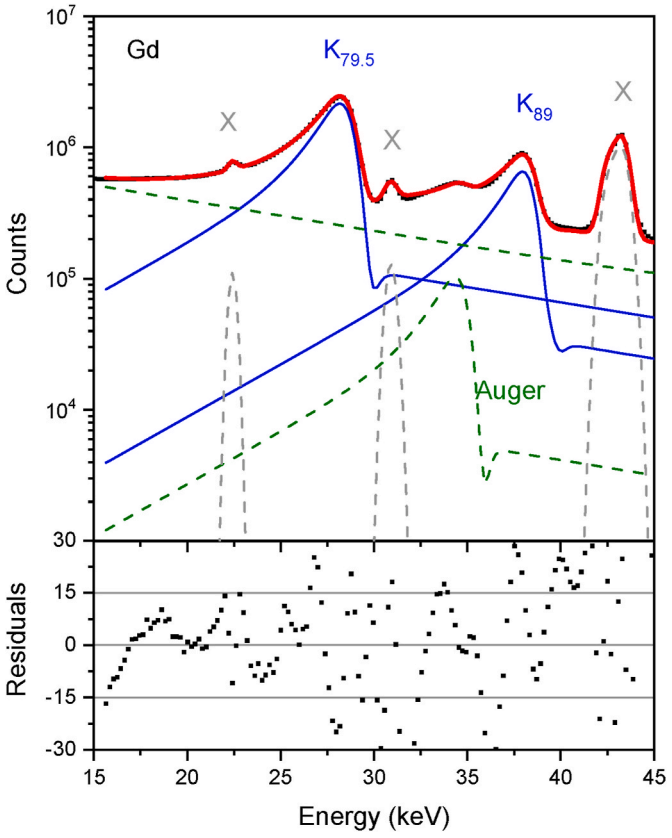

Fig. 5. Fit to the K ICE energy spectrum associated with the 79.51 keV and 88.967 keV transitions of ^{158}Gd and ^{156}Gd respectively. The additional lines show contributions from x rays, Auger electrons, and interfering parts of the spectrum, respectively.

from the 79.5 and 89 keV transitions. On top of that, the high continuum underneath the peaks can be reproduced by high-energy as well as low-energy tailing, thus any combination of those may result in somewhat different peak areas. A rather large uncertainty was assigned to the K peaks through the possible energy dependence of detection efficiency and the large continuum underneath the peaks (Table 2).

3.3. Discussion

Despite the significant uncertainty estimate, the K/L ICC ratios derived from the fitted peak areas (L/K = 1.55 (8) at 79.51 keV and 1.15 (14) at 89 keV) match the BrIcc data (1.50 and 1.15) (Table 2). The K ICE intensity diminishes visibly towards lower gamma transition energies since less energy is available to supersede the K electron binding energy. The L/M ratio of the fits is around 3, which is significantly lower than the value 4.2 from BrIcc. Also the L/N and L/O+ ratios are comparably low. It would appear that the M, N, O+ ICEs have higher intensities than expected from BrIcc. The O+ peaks are interfered by the gamma photon peaks and their area may be exaggerated due to spectral broadening. Fits to the single-pixel spectrum in Fig. 1 show lower O+ peaks, more in line with BrIcc.

Within the L shell, the fit confirms that L1 is much weaker than L3 (L1/L3 = 0.1), whereas L2 is only slightly smaller than L3 (L2/L3 = 0.9). The L1 peak of the 89 keV transition is strongly reduced in the fit, possibly because large part of its net peak area is misassigned to the interfering peak of the 79.5 keV gamma ray due to imperfections in the peak fitting. The energy resolution is not sufficient to disentangle unambiguously all peaks in the 80 keV region.

In Table 3, the L/K and L/M+ ICC ratios are compared to values published in the literature. The early work of Harms and McCormack (1974), cited by Kandlakunta et al. (2013), tabulates the ICE yields from the K, L, M+, shells for ^{158}Gd and ^{156}Gd. The quality of their energy spectrum was sufficient to distinguish these three major humps. More recently, Abdushukurov et al. (1994) published the K and L yields for ^{158}Gd in a paper describing the development of a generalised model for the efficiency of neutron detection using gadolinium as the converter material. The data from Harms and McCormack (1974) exhibit an expressed dominance of the L peak, resulting in significantly higher L/M+ and L/K values than BrIcc and this work, except for the L/K ratio from ^{156}Gd. Abdushukurov et al. (1994) also quote a significantly higher L/K value for ^{158}Gd. These discrepancies are likely to be consequential for detector design, particularly those sensitive to the lower energy emissions, such as the classes discussed in (Dumazert et al., 2018) and CMOS or hybrid sensors such as in (Pooley et al., 2017), where sensitivity to the 29 keV emission can be achieved via sensor modifications such as back-thinning.

4. Conclusions

The internal conversion electron spectrum emitted by neutron-irradiated natural gadolinium is of importance for its applications in neutron detectors and neutron capture therapy. An ICE energy spectrum was measured with a pixelated silicon detector and analysed with the software 'BEST'. The energy resolution of 1.8–1.9 keV at 72 keV –

Table 3
Comparison of the L/K and L/M+ ratios derived from this work and BrIcc with measurement results published in the literature: HAR-74 (Harms and McCormack, 1974; Kandlakunta et al., 2013) and ABD-94 (Abdushukurov et al., 1994).

Nucleus	Shell ratio	Energy [keV]	HAR-74	ABD-94	BrIcc	This work
^{158}Gd	L/K	71/29	2.73	2.05	1.50	1.55 (8)
	L/M+	71/78	4.34		3.38	2.37 (9)
^{156}Gd	L/K	81/39	1.19		1.15	1.14 (14)
	L/M+	81/88	4.28		3.38	2.24 (20)

currently the best result reported in the literature – allows for estimation of the contributions from major electron shells and from the L subshells. It is insufficient to disentangle the contributions from other subshells, considering the small spacing in binding energies. In comparison with the BrIcc data, higher yields are found from the M, N, O+ shells relatively to the dominant L ICE peaks, whereas within uncertainty no bias in the K ICE yields was found. The L subshell ratios are nearly consistent with BrIcc, although the L1 and L2 peaks appeared a bit smaller relative to L3.

CRediT authorship contribution statement

S. Pommé: Writing – original draft, Visualization, Software, Methodology, Formal analysis. **M.C. Veale:** Writing – review & editing, Resources, Investigation, Data curation, Conceptualization. **D.E. Pooley:** Writing – review & editing, Resources, Investigation, Conceptualization. **F. Van Assche:** Software, Resources. **F. Falksohn:** Formal analysis. **S.M. Collins:** Writing – review & editing, Formal analysis.

Declaration of competing interest

The authors declare that they have no known competing financial interests or personal relationships that could have appeared to influence the work reported in this paper.

Data availability

Data will be made available on request.

Acknowledgements

This research was funded by the UKRI STFC Centre for Instrumentation: Front End Electronics and Detectors for higher Energies and Rates (FEEDER) Managed Programme 2018–2022. Work performed by NPL was funded by the National Measurements System Programmes Unit of the UK's Department for Business, Energy and Industrial Strategy.

References

Abdushukurov, D.A., et al., 1994. Model calculation of efficiency of gadolinium-based converters of thermal neutrons. Nucl. Instrum. Methods B 84, 400–404.
Band, I.M., Trzhaskovskaya, M.B., Nestor Jr., C.W., Tikkanen, P.O., Raman, S., 2002. Dirac–Fock internal conversion coefficients. Atomic Data Nucl. Data Tables 81, 1–334.
Cerullo, N., Bufalino, D., Daquino, G., 2009. Progress in the use of gadolinium for NCT. Appl. Radiat. Isot. 67, S157–S160.
Cline, B., Bullough, M., Richardson, K., Thorpe, H., Veale, M.C., Wilson, M.D., 2022. Characterisation of the performance of p-type Si detectors for hard X-ray spectroscopy. J. Inst. Met. 17, P05030.
Dumazert, J., Coulon, R., Lecomte, Q., Bertrand, G.H.V., Hamel, M., 2018. Gadolinium for neutron detection in current nuclear instrumentation research: a review. Nucl. Instrum. Methods A 882, 53–68.
Dumazert, J., et al., 2020. Advancements in Gd-based neutron detection: γ–γ coincidence approach. Nucl. Instrum. Methods A 954, 161199.
Dumazert, J., et al., 2022. Advancements in Gd-based neutron detection (2): proton–gamma correlation approach. Nucl. Instrum. Methods A 1040, 167277.
García-Toraño, E., Crespo, T., Marouli, M., Jobbágy, V., Pommé, S., Ivanov, P., 2019. Alpha-particle emission probabilities of ^{231}Pa derived from first semiconductor spectrometric measurements. Appl. Radiat. Isot. 154, 108863.
Harms, A.A., McCormack, G., 1974. Isotopic conversion in gadolinium-exposure neutron imaging. Nucl. Instrum. Methods 118, 583–587.
Heenan, R.K., Penfold, J., King, S.M., 1997. SANS at pulsed neutron sources: present and future prospects. J. Appl. Crystallogr. 30, 1140–1147.
Kandlakunta, P., 2012. A Proof-Of-Principle Investigation for a Neutron-Gamma Discrimination Technique in a Semiconductor Neutron Detector Thesis. Graduate School of the Ohio State University.
Kandlakunta, P., Cao, L., 2012. Gamma-ray rejection, or detection, with gadolinium as a converter. Radiat. Protect. Dosim. 151, 586–590.
Kandlakunta, P., Cao, L.R., Mulligan, P., 2013. Measurement of internal conversion electrons from Gd neutron capture. Nucl. Instrum. Methods A 705, 36–41.
Kibédi, T., Burrows, T.W., Trzhaskovskaya, M.B., Davidson, P.M., Nestor Jr., C.W., 2008. Evaluation of theoretical conversion coefficients using BrIcc. Nucl. Instrum. Methods A 589, 202–229. Webinterface: http://bricc.anu.edu.au/index.php.
Lützenkirchen, K., et al., 2019. Analytical science of plutonium. In: Clark, D.L., Geeson, D.A., Hanraha Jr, R.J. (Eds.), Plutonium Handbook – Volume 4: Chemistry". American Nuclear Society, pp. 1808–1978, 2019.
Marouli, M., Pommé, S., Van Ammel, R., García-Toraño, E., Crespo, T., Pierre, S., 2017. Direct measurement of alpha emission probabilities in the decay of ^{226}Ra. Appl. Radiat. Isot. 125, 196–202.
Masaoka, S., Nakamura, T., Yamagishi, H., Soyama, K., 2003. Optimization of a micro-strip gas chamber as a two-dimensional neutron detector using gadolinium converter. Nucl. Instrum. Methods A 513, 538–549.
Narmani, A., et al., 2018. Gadolinium nanoparticles as diagnostic and therapeutic agents: their delivery systems in magnetic resonance imaging and neutron capture therapy. J. Drug Deliv. Sci. Technol. 44, 457–466.
Peräjärvi, K., Turunen, J., Ihantola, S., Kämäräinen, V., Pommé, S., Pöllänen, R., Siiskonen, T., Sipilä, H., Toivonen, H., 2014. Feasibility of conversion electron spectrometry using a Peltier-cooled silicon drift detector. J. Radioanal. Nucl. Chem. 299, 229–234.
Pfeifer, K.B., Achyuthan, K.E., Allen, M., Denton, M.L.B., Siegal, M.P., Manginell, R.P., 2017. Microfabrication of a gadolinium-derived solid-state sensor for thermal neutrons. J. Radiat. Res. 58, 464–473.
Pommé, S., Caro Marroyo, B., 2015. Improved peak shape fitting in alpha spectra. Appl. Radiat. Isot. 96, 148–153.
Pommé, S., 2015. Typical uncertainties in alpha-particle spectrometry. Metrologia 52, S146–S155.
Pommé, S., Paepen, J., Peräjärvi, K., Turunen, J., Pöllänen, R., 2016. Conversion electron spectrometry of Pu isotopes with a silicon drift detector. Appl. Radiat. Isot. 109, 183–188.
Pommé, S., Marouli, M., Paepen, J., Marković, N., Pöllänen, R., 2018. Deconvolution of ^{238,239,240}Pu conversion electron spectra measured with a silicon drift detector. Appl. Radiat. Isot. 134, 233–239.
Pommé, S., Paepen, Marouli, M., 2019. Conversion electron spectroscopy of the 59.54 keV transition in ^{241}Am alpha decay. Appl. Radiat. Isot. 153, 108848.
Pommé, S., 2022. Radionuclide metrology: confidence in radioactivity measurements. J. Radioanal. Nucl. Chem. 331, 4771–4798.
Pooley, D., et al., 2017. Development of the "GP2" detector: modification of the PImMS CMOS sensor for energy-resolved neutron radiography. IEEE Trans. Nucl. Sci. 64, 2970–2981.
Sakurai, Y., Kobayashi, T., 2002. Experimental Verification of the Nuclear Data of Gadolinium for Neutron Capture Therapy. J. Nucl. Sci. Technol. Suppl. 2, 1294–1297.
Tian, C., Zhu, L., Lin, F., Boyes, S.G., 2015. Poly(acrylic acid) bridged gadolinium metal–organic framework–gold nanoparticle composites as contrast agents for computed tomography and magnetic resonance bimodal imaging. ACS Appl. Mater. Interfaces 7, 17765–17775.
Van Assche, F., Vanheule, S., Van Hoorebeke, L., Boone, M.N., 2021. The spectral X-ray imaging data acquisition (SpeXIDAQ) framework. Sensors 21, 563.
Veale, M.C., Bell, S.J., Duarte, D.D., Schneider, A., Seller, P., Wilson, M.D., Iniewski, K., 2014. Measurements of charge sharing in small pixel CdTe detectors. Nucl. Instrum. Methods A. 767, 218–226.
Veale, M.C., Seller, P., Wilson, M., Liotti, E., 2018. HEXITEC: a high-energy X-ray spectroscopic imaging detector for synchrotron applications. Sync. Rad. News 31, 28–32.
Veale, M., et al., 2023. Development of a Novel Detector System for the Direct Measurement of the Electron and Photon Emissions from Gadolinium Following Neutron Capture. In preparation.